Local control of defects and switching properties in ferroelectric thin films

Sahar Saremi,[1] Ruijuan Xu,[1] Frances I. Allen,[1] Joshua Maher,[1] Joshua C. Agar,[1] Ran Gao,[1]
Peter Hosemann,[2] and Lane W. Martin[1,3,*]

[1]*Department of Materials Science and Engineering, University of California, Berkeley, California 94720, USA*
[2]*Department of Nuclear Engineering, University of California, Berkeley, California 94720, USA*
[3]*Materials Sciences Division, Lawrence Berkeley National Laboratory, Berkeley, California 94720, USA*

Electric-field switching of polarization is the building block of a wide variety of ferroelectric devices. In turn, understanding the factors affecting ferroelectric switching and developing routes to control it are of great technological significance. This work provides systematic experimental evidence of the role of defects in affecting ferroelectric-polarization switching and utilizes the ability to deterministically create and spatially locate point defects in $PbZr_{0.2}Ti_{0.8}O_3$ thin films via focused-helium-ion bombardment and the subsequent defect-polarization coupling as a knob for on-demand control of ferroelectric switching (e.g., coercivity and imprint). At intermediate ion doses (0.22–2.2×10^{14} ions cm^{-2}), the dominant defects (isolated point defects and small clusters) show a weak interaction with domain walls (pinning potentials from 200–500 K MV cm^{-1}), resulting in small and symmetric changes in the coercive field. At high doses (0.22–1×10^{15} ions cm^{-2}), on the other hand, the dominant defects (larger defect complexes and clusters) strongly pin domain-wall motion (pinning potentials from 500 to 1600 K MV cm^{-1}), resulting in a large increase in the coercivity and imprint, and a reduction in the polarization. This local control of ferroelectric switching provides a route to produce novel functions; namely, tunable multiple polarization states, rewritable pre-determined 180° domain patterns, and multiple zero-field piezoresponse and permittivity states. Such an approach opens up pathways to achieve multilevel data storage and logic, nonvolatile self-sensing shape-memory devices, and nonvolatile ferroelectric field-effect transistors.

I. INTRODUCTION

Electric-field switching of polarization between bistable states in ferroelectrics is the building block of a variety of applications, including memory, logic, energy storage and conversion, sensors, actuators, etc. [1–6]. Next-generation applications, however, are increasingly calling for the development of pathways to control ferroelectric switching beyond its bistable and degenerate nature. For example, establishing routes to access multiple polarization states can give rise to transformative changes in computation and data storage. Limited success, however, has been achieved in creating deterministically accessible and stable multi-states due to the intrinsically bistable and stochastic nature of ferroelectric switching [7–10]. In other applications, including ferroelectric field-effect transistors [11], micro-electro-mechanical systems [12], and shape-memory piezoelectric actuators [13], it is not only important to control the polarization state, but also to induce asymmetry of the ferroelectric states (manifested as an electrical imprint). Imprint in ferroelectrics, however, often appears in an uncontrolled fashion, arising from a number of factors (e.g., asymmetric electrodes, dead layers, trapped charges, and defects) [14–16] and there has been limited success in exerting on-demand control of imprinting [17,18]. In the end, addressing such technological challenges requires a comprehensive understanding of the ferroelectric switching process and all the factors that affect it, as well as developing pathways for deterministic and on-demand control of such factors. Such understanding and control, however, is challenging due to the complexity of the switching process and the multitude of both intrinsic (i.e., aspects of the material itself) and extrinsic (i.e., related to device structure) factors at play. While there has been excellent work in developing such understanding and control of these factors, considerable work still remains to provide the kind of on-demand control that is desired.

Among all the factors affecting switching, defects are known to play a prominent role whereby they control the thermodynamic stability of ferroelectric polarization, act as nucleation sites for switching, and serve as pinning sites for domain-wall motion [19]. Such defect-polarization coupling, in turn, can be used as a knob to manipulate the switching characteristics, provided there is an understanding of how specific defects affect the process and that there are approaches for the introduction of those specific defects with control over their concentration and location. Deterministic control of defects in such materials, however, has proven difficult. Complex-oxide ferroelectrics, for example, can accommodate a variety of *intrinsic* (i.e., related to the constituent elements) and *extrinsic* (i.e., related to the impurities and/or dopants present in the source materials) defects, which are often formed in an uncontrolled fashion. This lack of control over type, concentration, and position of defects has, in turn, hindered comprehensive, systematic, and quantitative studies of the nature of defect-polarization coupling, which ultimately limits

*lwmartin@berkeley.edu

their potential use for property control. In fact, most studies have been limited to the grown-in defects (thus lacking control over their type and concentration) or to those produced via chemical alloying (where the concentration is limited by the solid solubility and there can be simultaneous chemistry-induced changes in the ferroelectric properties which can obscure coupled effects) [8,20–24]. More recently, there have been attempts to implement, in ferroelectrics, approaches similar to the defect-engineering routes applied in modern semiconductors [25], including the use of ion bombardment or implantation to control the concentration of defects beyond the thermodynamic limit [26–28]. While such studies have relied on blanket ion bombardment, focused-ion-beam techniques provide a pathway to control the concentration and position of defects at nanometer and micrometer scales [29,30]. Such control over defect production, in turn, provides a new approach to the study of defect-polarization coupling in ferroelectrics. By providing pathways to both produce different types and concentrations (across many orders of magnitude of defect concentration) of defects and to position them in a controlled way, such techniques provide a framework in which systematic and quantitative studies of the interactions between defects and ferroelectric polarization can be accomplished and, ultimately, provide guidance for the development of new functionalities.

In this work, we focus on the prototypical tetragonal ferroelectric $PbZr_{0.2}Ti_{0.8}O_3$. The ferroelectric switching of $PbZr_{0.2}Ti_{0.8}O_3$ thin films is locally modified by the controlled introduction of defects using a focused-helium-ion beam. This enables the nature of the interplay between the induced defects and ferroelectric switching to be probed across three orders of magnitude of defect concentrations (10^{18}–10^{21} cm^{-3}). While there are no apparent changes at low doses (0.1–2.2 × 10^{13} ions cm^{-2}), transitioning to intermediate (0.22–2.2 × 10^{14} ions cm^{-2}) and high (0.22–1 × 10^{15} ions cm^{-2}) doses does affect the switching. At intermediate doses, a relatively small and symmetric increase in the coercivity is observed and is attributed to increasing densities of isolated point defects and small clusters which exhibit a weak defect-polarization coupling (pinning energies between 200–500 K MV cm^{-1}). At high doses, a large increase in the coercivity and imprint, and a reduction in the polarization are observed. This increase in the strength of defect-polarization interactions is attributed to the formation of larger defect complexes and clusters, which have a much stronger defect-pinning potential (500–1600 K MV cm^{-1}). In turn, it is shown that such defect-induced changes can be confined to selected regions defined by the ion beam and can be used to realize novel functions; namely, tunable multiple polarization states, rewritable pre-determined 180° domain patterns, and multiple, zero-field-permittivity and piezoresponse states in an intrinsically bistable ferroelectric.

II. METHODS

A. Heterostructure growth

Heterostructures were grown via pulsed-laser deposition using a KrF excimer laser (248 nm, Compex, Coherent) in an on-axis geometry. Sixty-nm-thick $PbZr_{0.2}Ti_{0.8}O_3$ films were grown on 20 nm $SrRuO_3$/$SrTiO_3$ (001) single-crystal substrates (Crystec, GmbH) from ceramic targets. The $SrRuO_3$

layer, to be used as a bottom electrode for subsequent electrical studies, was grown at a temperature of 690 °C in a dynamic oxygen pressure of 100 mTorr at a laser repetition rate of 15 Hz and a laser fluence of 1.3 J cm^{-2}. The $PbZr_{0.2}Ti_{0.8}O_3$ films were grown at a temperature of 650 °C in a dynamic oxygen pressure of 200 mTorr at a laser repetition rate of 3 Hz, and a laser fluence of 1.0 J cm^{-2}. Following growth, the heterostructures were cooled to room temperature at a rate of 10 °C min^{-1} in a static oxygen pressure of 700 Torr. To enable the subsequent measurement of dielectric and ferroelectric properties, top $SrRuO_3$ electrodes with a thickness of 60 nm were patterned by using a MgO hard-mask in a circular shape with diameter of 25 μm [31].

B. Ion bombardment and defect creation

Following growth, a Zeiss ORION NanoFab microscope was used to bombard the heterostructures and to produce defects in select regions. All bombardment experiments were carried out at room temperature, using a 25 keV, $\sim$2 pA He$^+$-ion beam with a nominal probe size of 0.5 nm (10 μm aperture, spot 4, working distance 9 mm) under normal incidence. The high-spatial resolution of the focused-helium-ion beam was used for positioning of the defects with nanometer-scale precision. The concentration of induced defects was systematically controlled by varying the bombardment dose in the range of 10^{12} to 10^{15} ions cm^{-2}. Regions of interest for ion bombardment were located under low-dose imaging conditions (10^9 ions cm^{-2}, at least three orders of magnitude lower than the lowest dose used in this study), and the patterning was performed using the NPVE software (Fibics, Inc.) selecting a pixel dwell time of 1 μs and a pixel spacing of typically 0.25 nm.

To gain information about the concentration profile of the bombardment-induced defects and implanted ions as a function of the film thickness, stopping and range of ions in matter (SRIM) simulations [32] were performed by using the program SRIM 2013 (srim.org). SRIM is a group of programs that calculate the stopping and range of ions in matter by using a Monte Carlo method. Complex targets made of compound materials with up to eight layers can be defined, and final three-dimensional (3D) distribution of the ions, target damage, sputtering, ionization, and phonon production can be simulated. In this work, SRIM simulations were performed using a displacement energy of 25 keV in the Kinchin–Pease mode.

C. Structural, chemical, and physical property characterization

Following growth, the crystalline structure of the films was probed by x-ray diffraction using a Panalytical X'Pert^3 MRD 4-circle diffractometer. The chemistry was probed via Rutherford backscattering spectrometry with a He^{2+}-ion energy of 3040 keV, an incident angle $\alpha = 22.5°$, an exit angle $\beta = 25.35°$, and a scattering angle $\theta = 168°$, in the Cornell geometry. Fits to the experimental data were completed using the analysis software SIMNRA (simnra.com).

Following ion bombardment, and to understand the effect of bombardment-induced defects on properties, various capacitor-based dielectric and ferroelectric measurements were carried out at varying ion doses. The dielectric properties were measured by using an impedance analyzer (E4990A,

Keysight) as a function of dc bias at a frequency of 1 kHz and an excitation voltage of 15 mV. Ferroelectric measurements were conducted using a Precision Multiferroic Tester (Radiant Technologies). Ferroelectric hysteresis loops were obtained using a bipolar triangular voltage profile. Macroscale switching-kinetics studies were performed using standard pulse measurements (Supplemental Material, Fig. S1 [33]) in which the change of polarization is probed as a function of pulse width and amplitude. Positive-up-negative-down (PUND) measurements, in which the change of polarization is measured as a function of pulse voltage at a constant pulse width, were carried out using a modified PUND pulse sequence (Supplemental Material, Fig. S2 [33]). Retention measurements, which probe the variation of switched polarization as a function of time, were conducted using a standard retention pulse sequence (Supplemental Material, Fig. S3 [33]). First-order reversal curve (FORC) analyses, which involve the measurement of hysteresis loops between the saturation field and various reversal fields, were performed to probe the distribution of the elementary switchable units over their coercive and bias fields [34]. The FORC measurements were conducted by measuring multiple minor loops at 1 kHz using a monopolar triangular voltage profile, between a negative saturation field and a variable reversal field E_r, and FORC distributions were determined by using established numerical methods [35] (Supplemental Material [33]).

D. Piezoresponse force microscopy and band-excitation piezoresponse spectroscopy

Piezoresponse force microscopy (PFM) studies were carried out by using a MFP-3D AFM (Asylum Research) using Ir/Pt-coated conductive tips (Nanosensor, PPP-EFM, force constant ≈ 2.8 N m^{-1}). Band-excitation piezoresponse spectroscopy (BEPS) studies were performed at the Center for Nanophase Materials Science (CNMS) at Oak Ridge National Laboratory (ORNL) using a custom Cypher (Asylum Research) atomic force microscope. BEPS is a multifrequency technique [36] wherein the piezoresponse is measured by using a band-excitation waveform at remanence throughout a bipolar triangular switching waveform (Supplemental Material, Fig. S4 [33]). All measurements were undertaken using Pt/Ir-coated conductive tips (NanoSensor PPP-EFM, force constant ≈ 2.8 N m^{-1}). The cantilever response was measured in the time domain at remanence at various voltage steps throughout a bipolar-triangular switching waveform. The magnitude of the waveform was chosen to be large enough to fully saturate the piezoelectric hysteresis loops. The local piezoresponse was measured at remanence (following a dwell time of 0.5 ms), with a band-excitation waveform of sinc character (peak-to-peak voltage of 1 V). Details of the loop fitting procedure for the band excitation—which is critical to extract quantitative information from this approach—is also provided (Supplemental Material [33]).

III. RESULTS AND DISCUSSION

X-ray diffraction studies of the as-grown heterostructures reveal that the films are fully epitaxial and single-phase (Supplemental Material, Fig. S5(a) [33]) and chemical analysis via Rutherford backscattering spectrometry reveals that the films

are stoichiometric (Supplemental Material, Fig. S5(b) [33]). Subsequent ion-bombardment experiments were carried out on these heterostructures using varying bombardment doses in the range of 10^{12} to 10^{15} ions cm^{-2}. SRIM simulations suggest that lead, titanium, zirconium, and oxygen vacancies, resulting from collisions between the incoming helium ions and the target atoms, form with relatively uniform concentrations (in the range of 10^{18} to 10^{21} cm^{-3}) throughout the thickness of the ferroelectric layer (Supplemental Material, Fig. S6(a) [33]). In addition to the formation of *intrinsic* point defects, helium ions are also implanted into the heterostructures (Supplemental Material, Fig. S6(b) [33]). The concentration of the helium ions, however, is more than three orders of magnitude smaller than the *intrinsic* point-defect concentration (Supplemental Material, Fig. S6(c) [33]), suggesting that the observed defect-induced effects are predominantly induced by the *intrinsic* defects. Comparison of the surface topography before and after ion bombardment to a dose of 10^{15} ions cm^{-2} reveals no signature of formation of helium bubbles and blisters (Supplemental Material, Fig. S7 [33]), which are known to form at higher doses [37].

To study the effect of the induced defects on ferroelectric switching, various ion-bombardment procedures were undertaken on the capacitor structures. First, the helium-ion beam was rastered over multiple capacitors at varying doses to prepare capacitors with systematically increasing defect concentrations. Ferroelectric hysteresis loops were measured before and after ion bombardment. All as-grown capacitors showed symmetric, low-leakage hysteresis loops, with similar remanent polarization and coercive fields (~ 70 μC cm^{-2} and ~ 110 kV cm^{-1}, respectively) (Supplemental Material, Fig. S8 [33]). Following ion bombardment, marked changes in the hysteresis loops were observed [Fig. 1(a)]. To quantify these changes, the average coercive field (i.e., $E_C = (|E_C^+| + |E_C^-|)/2$, where E_C^+ and E_C^- are the coercive fields for the positive and negative voltages, respectively), imprint (i.e., $(|E_C^+| - |E_C^-|)/2$), and average saturation polarization [$P_S = (|P_s^+| + |P_s^-|)/2$ where P_s^+ and P_s^- are the saturation polarization under positive and negative voltages, respectively] were extracted as a function of dose [Fig. 1(b)]. Based on this analysis, three regimes can be identified: (1) At low doses (0.1–2.2×10^{13} ions cm^{-2}) there is effectively no change in the hysteresis loops. (2) At intermediate doses (0.22–2.2×10^{14} ions cm^{-2}) a relatively small increase in the coercivity is observed, while there is effectively no change in either the imprint or the polarization. (3) At high doses (0.22–1×10^{15} ions cm^{-2}) there are large increases in the coercivity and imprint, and a reduction in the polarization.

To understand these observations, macroscale switching-kinetics studies were performed at varying doses, in which the change of polarization was probed as a function of pulse width and amplitude (Supplemental Material, Fig. S9 [33]). The Kolmogorov–Avrami–Ishibashi (KAI) model [38,39] was used to fit the experimental data (Supplemental Material [33]), and to extract the switching speed (ϑ) as a function of applied electric field E (Supplemental Material, Table SI [33]). Using this approach, the domain-wall motion can be classified into creep, depinning, and flow regimes [40]. Linear variation of $\ln(\vartheta)$ with E^{-1} in these heterostructures reveals that, for all doses, the domain-wall motion is in the creep regime [inset,
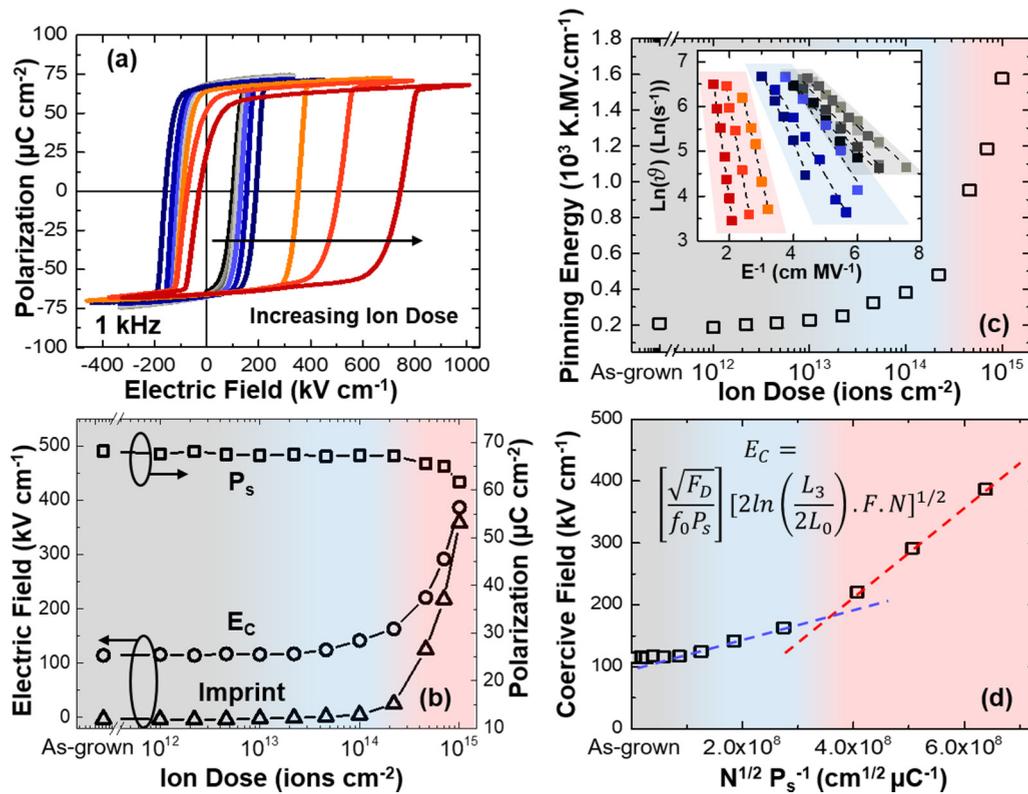
FIG. 1. (a) Polarization-electric field hysteresis loops for capacitors exposed to ion-bombardment doses from 10^{12} to 10^{15} ions cm^{-2}. (b) Evolution of the ferroelectric switching characteristics including the saturation polarization (P_S), coercive field (E_C), and imprint with ion dose. (c) Evolution of the extracted defect-pinning energy as a function of ion dose; inset shows the evolution of the switching speed as a function of inverse electric field with ion dose. The pinning energy is extracted from the slope of the linear fits. (d) Evolution of the coercive field as a function of defect concentration; inset shows the mathematical relationship between defect concentration and coercive field.

Fig. 1(c)]. The pinning energies for the creep motion, which involves thermally activated propagation of domain walls between pinning sites, are extracted from the slope of the linear fits [Fig. 1(c)]. Different creep behavior is observed in the three dose regimes. In the low-dose regime, no change in the pinning energy is observed (∼200 K MV cm^{-1}). In the intermediate-dose regime, the pinning energy increases up to ∼500 K MV cm^{-1}. Finally, in the high-dose regime, there is a large increase in the pining energy up to ∼1600 K MV cm^{-1}.

It is hypothesized that, in the low-dose regime, the bombardment-induced defects are of the same order of magnitude as the as-grown defects and, therefore, do not give rise to marked changes. In the intermediate- and high-dose regimes, the induced defects start to interact with the domain walls. The nature and strength of this interaction, however, is different due to the difference in the dominant type of defects in these regimes. Experimental and theoretical studies of defect-domain-wall interactions suggest that point defects are more stable at the domain walls and can pin their motion [41,42]. The pinning strength, however, is shown to be different for different defect types. A large difference, for example, is reported between isolated point defects and defect complexes, the latter showing at least three-times higher pinning strengths [41]. In addition, defect complexes (which can possess a dipole moment) have a strong tendency to align in the polarization direction and break the degeneracy of polarization states [14,20,41–44]. Moreover, the coercive field has been modeled

in terms of the microstructure of the domain walls and the number and pinning strength of the lattice defects by using the following equation [45]:

$$E_C = \left[\frac{\sqrt{F_D}}{f_0 P_s}\right]\left[2\ln\left(\frac{L_3}{2L_0}\right)FN\right]^{1/2}, \quad (1)$$

where E_C is the coercive field, F_D is the area of the domain walls, P_s is the spontaneous polarization, f_0 is a geometrical factor depending on the angle between the electric field, L_3 is the average distance between the domain walls, L_0 is the average distance between the points of zero force encountered by a domain wall, F is the pinning strength of the defects, and N is the defect concentration. According to this model, the coercivity is proportional to the square root of the defect concentration ($N^{1/2}$), given the microstructure of the domain walls and strength of defect-domain-wall interactions is constant [45]. The concentration of the initial bombardment-induced point defects at various doses can be approximated using SRIM simulations (Supplemental Material, Fig. S6(a) [33]). In our case, the variation of coercive field is plotted as a function of $N^{1/2}P_s^{-1}$ (to account for the variation of polarization at high doses) and shows three distinct slopes [Fig. 1(d)]. Again, in the low-dose regime, there is no change in the coercivity. Within the intermediate- and high-dose regimes, the coercivity varies linearly with $N^{1/2}$, but with two different slopes. This change of slope can be attributed to the
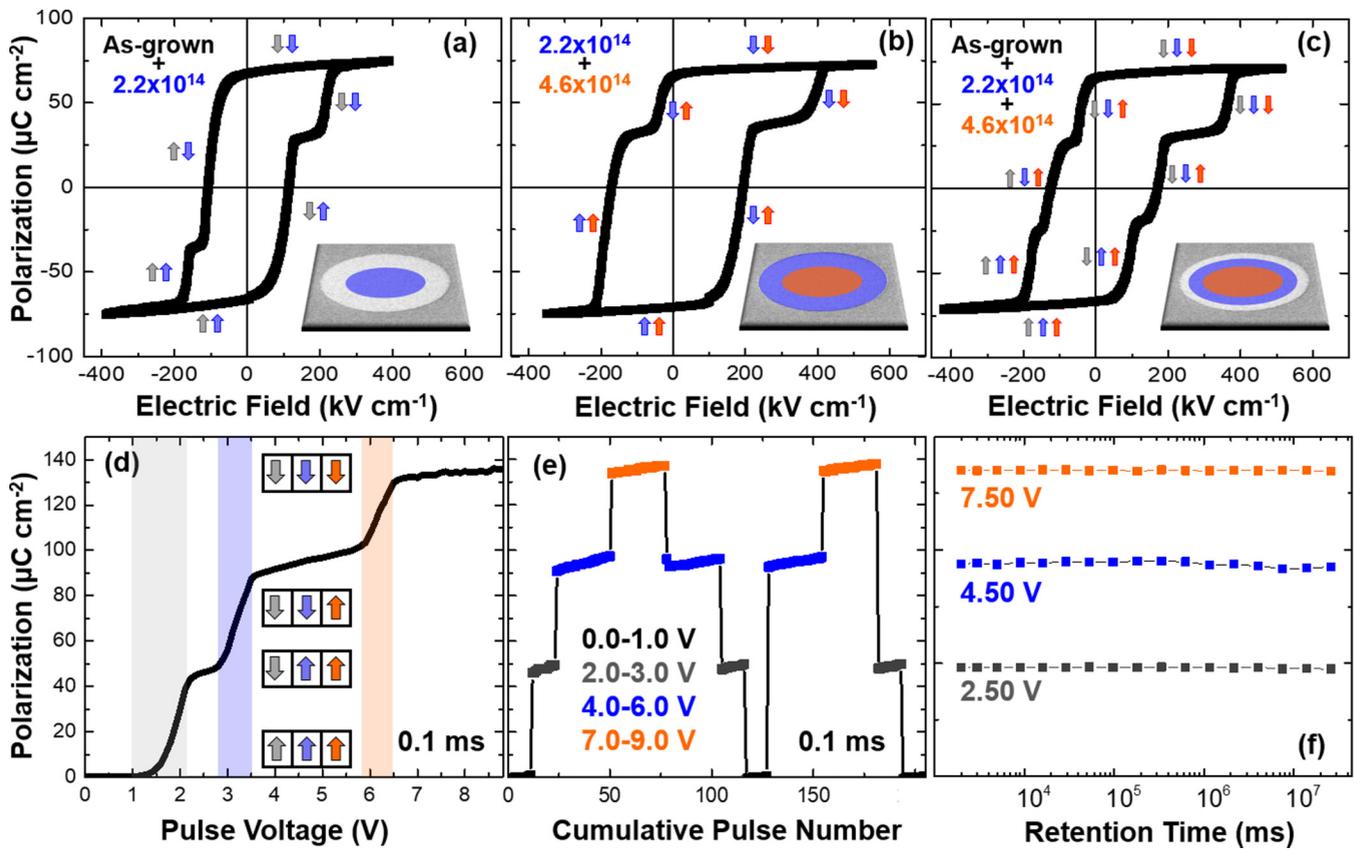
FIG. 2. Polarization-electric field hysteresis loops for capacitors exposed to various ion-bombardment procedures including (a) as-grown (gray region) and 2.2×10^{14} ions cm^{-2} (blue region) resulting in symmetric two-step switching, (b) 2.2×10^{14} ions cm^{-2} (blue region) and 4.6×10^{14} ions cm^{-2} (red region) resulting in asymmetric two-step switching, and (c) as-grown (no bombardment, gray region), 2.2×10^{14} ions cm^{-2} (blue region), and 4.6×10^{14} ions cm^{-2} (red region) resulting in three-step switching. Focusing on the capacitors in (c), subsequent (d) PUND studies reveal the pathway to the different polarization states at a constant pulse width of 0.1 ms, (e) the ability to deterministically switch between the different polarization states, and (f) the long-term retention and stability of the multiple polarization states.

difference in the pinning-strength F of the dominant defects. This correlates with the evolution of bombardment-induced defects which need to overcome a critical size to grow. At an initial stage, one increases the number of critical defects, whereas at higher doses they cluster and grow. Therefore, we conclude that, in the intermediate-dose regime, the dominant defects are likely isolated-point defects and small clusters with a low pinning strength, which results only in a small increase in the pinning energy and coercivity. On the other hand, within the high-dose regime larger complexes and clusters are likely to form and their stronger pinning strength drives a rapid increase of the pinning energy and coercivity. In addition, the increase of imprint and reduction of polarization within the high-dose regime suggests the presence of a preferred polarization direction, further supporting the idea that defect-complexes are playing a dominant role. This work, therefore, provides systematic experimental evidence of the role of different defect types (i.e., isolated point defects and complexes or clusters) in affecting ferroelectric-polarization switching.

In the following, we show that the presence of this defect-polarization coupling, and the ability to control the type, concentration, and location of defects via focused-ion beams, allows one to realize new functionalities. First, we show that local control over the coercivity can provide an effective

pathway for creating multi-state switching processes in intrinsically bistable ferroelectrics. To achieve this, different regions of single capacitors are bombarded with different doses. In one capacitor, the ion beam is rastered over one-third of the total area (central region) to produce an intermediate dose (2.2×10^{14} ions cm^{-2}), leaving two-thirds of the capacitor (outer region) in the as-grown state [Fig. 2(a)]. These regions, therefore, are expected to have different coercivities. Under lower voltages, only the as-grown region (two-thirds of the polarization) is switched. The bombarded region (and the remaining one-third of the polarization) switches only once the electric field exceeds its corresponding coercive field, and consequently, two-step switching is realized. The same process repeats itself under the opposite bias. In another capacitor, a different dose combination is used [Fig. 2(b)] wherein the beam is rastered over the entire capacitor to produce an intermediate dose (2.2×10^{14} ions cm^{-2}) before being further rastered over one-third of the capacitor (central region) to produce a high dose (4.6×10^{14} ions cm^{-2}). In this case, for switching from negative to positive polarization, the intermediate-dose region switches first, followed by the high-dose region at a larger field. In the opposite direction, however, the sequence of the two-step switching is reversed, due to the induced imprint in the high-dose region. Finally, another capacitor was created
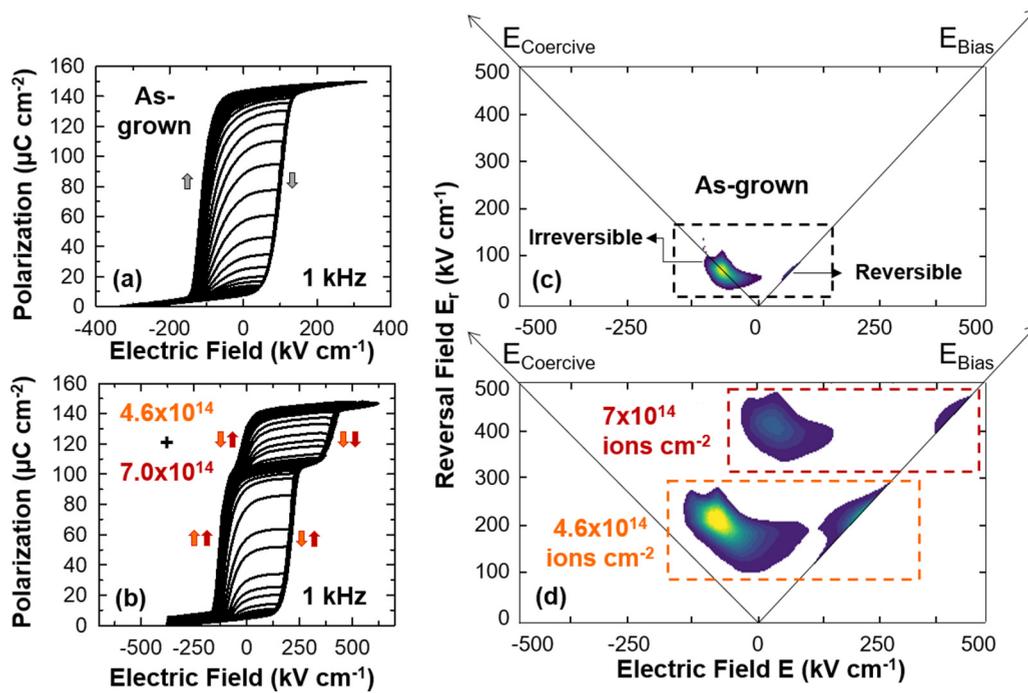
FIG. 3. Polarization-electric field hysteresis loops taken between a negative saturation field and various positive reversal fields for (a) as-grown and (b) 4.6×10^{14} and 7.0×10^{14} ions cm^{-2} two-region ion-bombarded capacitors. Analysis of the FORC data reveals the distribution of elementary switchable units over their coercive and bias fields for the (c) as-grown and (d) 4.6×10^{14} and 7.0×10^{14} ions cm^{-2} two-region ion-bombarded capacitors.

wherein the beam was rastered to create three regions of equal area: (1) no ion bombardment (outer region), (2) intermediate dose (2.2×10^{14} ions cm^{-2}, middle region), and (3) high dose (4.6×10^{14} ions cm^{-2}, central region). Consequently, three-step switching processes are observed resulting in four polarization states [Fig. 2(c)]. Therefore, the shape of the hysteresis loops, the number of states, their polarization values, and voltage-range stability can be engineered by choosing different dose combinations and volume ratios.

To probe the utility and robustness of this process, a capacitor exhibiting three-step switching [Fig. 2(c)] was studied using PUND measurements. The voltage stability range of each state is extracted [Fig. 2(d)] and used to demonstrate arbitrary access to each state in an on-demand fashion [Fig. 2(e)]. The possible states are accessed in an ascending, descending, and random order by controlling the pulse voltage. The stability of the polarization states was probed by studying the variation of remanent polarization with time [Fig. 2(f)] using a retention pulse sequence. Each polarization state is accessed using the appropriate pulse width and voltage and read after gradually increasing retention times. All the states are stable over time, showing no loss of polarization after ~7 hours (separate studies performed weeks later also show no loss of the written states). Therefore, nonvolatile and deterministically accessible multi-states can be produced, opening the door to multilevel data storage and logic.

To study the microscopic mechanisms involved in the switching process, and their (in)homogeneity, FORC studies were performed on as-grown capacitors [Fig. 3(a)] and capacitors bombarded with two doses of 4.6×10^{14} and 7.0×10^{14} ions cm^{-2} [Fig. 3(b)]. The contour plots of the distribution

functions (Supplemental Material [33]) are shown [Figs. 3(c) and 3(d)]. The distributions along the bias and coercive-field axes correspond to the reversible and irreversible contributions to the total polarization, respectively [33]. Focusing on the irreversible contributions, the as-grown capacitor reveals a single distribution over a small coercive field and a zero-bias field [Fig. 3(c)]. The same measurement on capacitors bombarded with two doses reveals two distinct distributions, showing that increasing the dose shifts the distribution to higher coercive and bias fields, and that this shift can be confined to certain regions.

Scanning-probe microscopy further supports our proposed mechanism for the observed multi-state switching. BEPS measurements were performed by using a band-excitation waveform at remanence throughout a bipolar triangular switching waveform [Fig. 4(a)], on a region bombarded with three doses: zero, 2.2×10^{14}, and 10^{15} ions cm^{-2}. A movie of the switching is constructed by forming phase images at each voltage step throughout the switching waveform. A few snapshots (phase images) during the switching are provided [Fig. 4(b)]. At zero voltage (V_0) the entire region has an upward polarization. At voltage $+V_1$, which is larger than the coercivity of the as-grown region, but smaller than that of the bombarded regions, only the as-grown region switches. The switching proceeds by switching of the regions bombarded with doses of 2.2×10^{14} and 10^{15} ions cm^{-2} at voltages of $+V_2$ and $+V_3$, respectively. This shows the step-by-step nature of the switching, and that the defects and their induced effects can be confined to select regions defined by the ion beam. Further quantification of the results (Supplemental Material [33]) also reveals a dose-dependent increase in the coercive field of the average
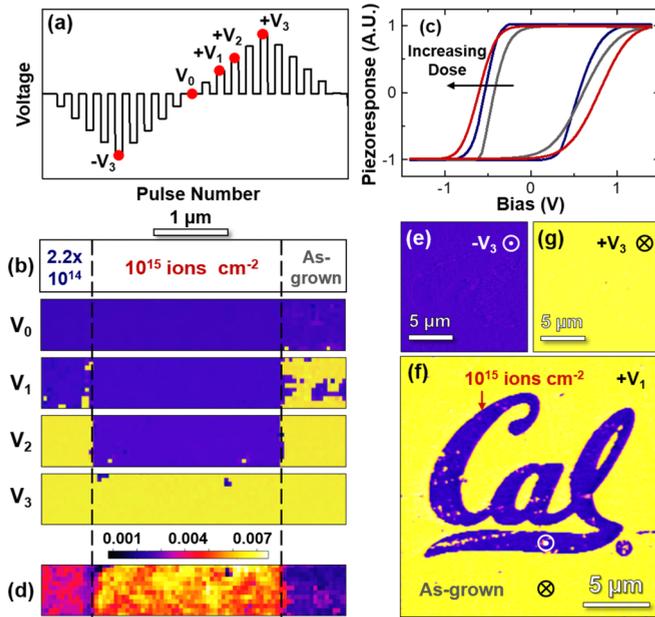
FIG. 4. (a) Schematic of the probing waveform used for BEPS measurements. The piezoresponse is measured at remanence. (b) (top) Schematic of the entire region studied herein, including the doses used in each area, as well as the phase response at different voltages (V_0, V_1, V_2, and V_3) showing the step-by-step nature of the switching. (c) Average piezoresponse loops extracted from each region in panel (b). (d) Extracted work of switching (defined as the area within the piezoelectric loops) for each region. PFM phase images of the (e) as-poled ($-V_3$), (f) the partially switched ($+V_1$), and (g) fully switched same areas showing the ability to deterministically write defects to produce domain structures.
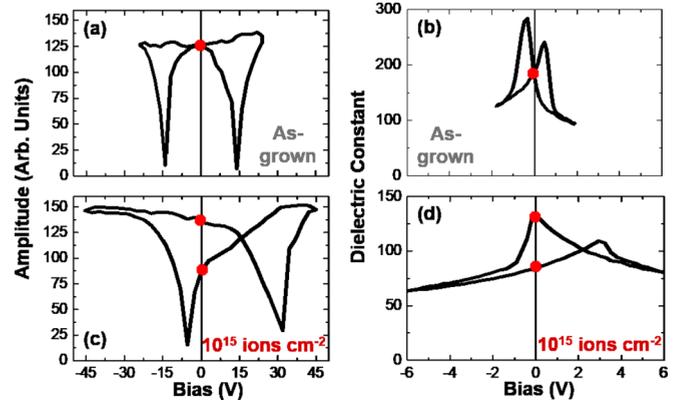

FIG. 5. (a) Piezoresponse amplitude as extracted from PFM studies and (b) dielectric permittivity (constant) as a function of applied bias for as-grown capacitors. (c) Piezoresponse amplitude as extracted from PFM studies and (d) dielectric permittivity (constant) as a function of applied bias for 10^{15} ions cm^{-2} ion-bombarded capacitors.

piezoelectric loops [Fig. 4(c)], and the "work of switching" [Fig. 4(d)], which is consistent with other experimental data in this work, showing an increase in the coercivity with increasing defect concentration, as a result of defect pinning.

Motivated by the ability to locally manipulate the coercivity, we examined the possibility of creating arbitrary 180° domain patterns. Selective regions of the film were bombarded with a dose of 10^{15} ions cm^{-2} in the form of the Cal™ logo. A $15 \times 15\,\mu$m region containing the bombarded area and its as-grown background was then poled to an upward direction using PFM [Fig. 4(e)]. Afterwards, a small positive voltage $+V_1$ (only sufficient to switch the as-grown region) is applied to the entire area. The logo appears (still unswitched) after this step with a 180° contrast from its background [Fig. 4(f)]. Applying a positive voltage higher than the coercivity of the bombarded region ($+V_3$) switches the entire area to a down-poled polarization and the logo disappears [Fig. 4(g)]. Therefore, predetermined and rewritable 180° domain patterns can be written, with feature sizes being limited only by the size and interaction volume of the ion beam.

As mentioned previously, the dose-dependent increase in the coercivity is accompanied by an increase of electrical imprint in the high-dose regime due to the formation of defect complexes and clusters. Here, we demonstrate that the dose dependence of imprint can also be used to modify the function and can be useful for any application where stabilizing the ferro-

electric polarization in one direction is beneficial. For example, imprint is important in ferroelectric field-effect transistors (to address retention issues) [11,18] and gives rise to asymmetry in strain and permittivity responses which are useful for self-sensing shape-memory piezoelectric actuators [13,17,46]. Here, we observe that the imprint associated with ion bombardment can give rise to features in both the piezoresponse and permittivity, suggesting that such processing approaches can be useful for deterministically tuning devices used for these applications. For example, in both local piezoresponse [Fig. 5(a)] and dielectric permittivity measurements [Fig. 5(b)], the as-grown capacitors show only one stable state at zero field. After ion bombardment (10^{15} ions cm^{-2}), the defect-induced imprint means that multiple zero-field states are realized with the reversal of polarization in both the piezoresponse [Fig. 5(c)] and permittivity [Fig. 5(d)]. In turn, such memory effects can be used for self-sensing operation and position detection in shape-memory piezoelectrics [13,17,46].

IV. CONCLUSIONS

In conclusion, we show that on-demand tuning of type, concentration, and position of defects can provide a powerful tool for the systematic and quantitative study of defect-polarization interactions and enables a deterministic control of the switching properties in ferroelectric thin films. For example, the coercivity and imprint characteristics can be tuned in selected regions by using focused-ion beams. We show that this control is the result of interactions between defects and domain walls, and that the strength of these interactions is strongly dependent on the defect type and concentration. While isolated-point defects and small clusters show a weak interaction with the domain walls (pinning potentials from 200 to 500 K MV cm^{-1}) and give rise to a relatively small and symmetric increase in the coercivity, larger complexes and clusters strongly pin the domain-wall motion (pinning potentials from 500 to 1600 K MV cm^{-1}) and give rise to a large increase in the coercivity and a preferred polarization direction (manifested as an electrical imprint and a reduction in the polarization). Using the ability to manipulate the coercivity in select regions,

we demonstrate multiple stable states in an otherwise bistable ferroelectric, where the number of states, their polarization values, and switching voltages can be varied systematically. We also demonstrate the potential of this technique for creating rewritable predetermined 180° domain patterns. Finally, we demonstrate controllable electrical imprint which can give rise to multiple zero-field dielectric and piezo responses.

ACKNOWLEDGMENTS

[1] M. E. Lines and A. M. Glass, *Principles and Applications of Ferroelectrics and Related Materials* (Clarendon, Oxford, 1977).

[2] J. F. Scott, *Ferroelectric Memories* (Springer, Germany, 2000).

[3] P. Muralt, Ferroelectric thin films for micro-sensors and actuators: a review, J. Micromech. Microeng. **10**, 136 (2000).

[4] C.R. Bowen, J. Taylor, E. LeBoulbar, D. Zabek, A. Chauhan, and R. Vaish, Pyroelectric materials and devices for energy harvesting applications, Energy Environ. Sci. **7**, 3836 (2014).

[5] A. R. Damodaran, J. C. Agar, S. Pandya, Z. Chen, L. R. Dedon, R. Xu, B. Apgar, S. Saremi, and L. W. Martin, New modalities of strain-control of ferroelectric thin films, J. Phys.: Condens. Matter **28**, 263001 (2016).

[6] J. C. Agar, S. Pandya, R. Xu, A. K. Yadav, Z. Liu, T. Angsten, S. Saremi, M. Asta, R. Ramesh, and L. W. Martin, Frontiers in strain-engineered multifunctional ferroic materials, MRS Commun. **6**, 151 (2016).

[7] M. H. Park, H. J. Lee, G. H. Kim, Y. J. Kim, J. H. Kim, J. H. Lee, and Ch. S. Hwang, Tristate memory using ferroelectric-insulator-semiconductor heterojunctions for 50% increased data storage, Adv. Funct. Mater. **21**, 4305 (2011).

[8] D. Lee, B. C. Jeon, S. H. Baek, S. M. Yang, Y. J. Shin, T. H. Kim, Y. S. Kim, J.-G. Yoon, C. B. Eom, and T. W. Noh, Active control of ferroelectric switching using defect-dipole engineering, Adv. Mater. **24**, 6490 (2012).

[9] A. Ghosh, G. Koster, and G. Rijnders, Multistability in bistable ferroelectric materials toward adaptive applications, Adv. Funct. Mater. **26**, 5748 (2016).

[10] L. Baudry, I. Lukyanchuk, and V. M. Vinokur, Ferroelectric symmetry-protected multibit memory cell, Sci. Rep. **7**, 42196 (2017).

[11] T. Ma, and J.-P. Han, Why is nonvolatile ferroelectric memory field-effect transistor still elusive? IEEE Electron Device Lett. **23**, 386 (2002).

[12] S. Baek, J. Park, D. Kim, V. Aksyuk, R. Das, S. Bu, D. Felker, J. Lettieri, V. Vaithyanathan, and S. Bharadwaja, Giant piezoelectricity on Si for hyperactive MEMS, Science **334**, 958 (2011).

[13] T. Morita, Y. Kadota, and H. Hosaka, Shape memory piezoelectric actuator, Appl. Phys. Lett. **90**, 082909 (2007).

[14] G. Arlt, and H. Neumann, Internal bias in ferroelectric ceramics: Origin and time dependence, Ferroelectrics **87**, 109 (1988).

[15] W. L. Warren, B. A. Tuttle, D. Dimos, G. E. Pike, H. N. Al-Shareef, R. Ramesh, and J. T. Evans, Imprint in ferroelectric capacitors, Jpn. J. Appl. Phys. **35**, 1521 (1996).

[16] A. K. Tagantsev, and G. Gerra, Interface-induced phenomena in polarization response of ferroelectric thin films, J. Appl. Phys. **100**, 051607 (2006).

[17] W.-H. Kim, J. Y. Son, Y.-H. Shin, and H. M. Jang, Imprint control of nonvolatile shape memory with asymmetric ferroelectric multilayers, Chem. Mater. **26**, 6911 (2014).

[18] A. Ghosh, G. Koster, and G. Rijnders, Tunable and stable in time ferroelectric imprint through polarization coupling, APL Mater. **4**, 066103 (2016).

[19] S. M. Yang, J.-G. Yoon, and T. W. Noh, Nanoscale studies of defect-mediated polarization switching dynamics in ferroelectric thin film capacitors, Curr. Appl. Phys. **11**, 1111 (2011).

[20] X. Ren, Large electric-field-induced strain in ferroelectric crystals by point-defect-mediated reversible domain switching, Nat. Mater. **3**, 91 (2004).

[21] S. Zhang, R. E. Eitel, C. A. Randall, T. R. Shrout, and E. F. Alberta, Manganese-modified $BiScO_3$–$PbTiO_3$ piezoelectric ceramic for high-temperature shear mode sensor, Appl. Phys. Lett. **86**, 262904 (2005).

[22] A. R. Damodaran, E. Breckenfeld, Z. Chen, S. Lee, and L. W. Martin, Enhancement of ferroelectric Curie temperature in $BaTiO_3$ films via strain-induced defect dipole alignment, Adv. Mater. **26**, 6341 (2014).

[23] L. R. Dedon, S. Saremi, Z. Chen, A. R. Damodaran, B. A. Apgar, R. Gao, and L. W. Martin, Nonstoichiometry, structure, and properties of $BiFeO_3$ films, Chem. Mater. **28**, 5952 (2016).

[24] R. Gao, S. E. Reyes-Lillo, R. Xu, A. Dasgupta, Y. Dong, L. R. Dedon, J. Kim, S. Saremi, Z. Chen, C. R. Serrao, H. Zhou, J. B. Neaton, and L. W. Martin, Ferroelectricity in $Pb_{1+\delta}ZrO_3$ thin films, Chem. Mater. **29**, 6544 (2017).

[25] S. Saremi, R. Gao, A. Dasgupta, and L. W. Martin, New facets for the role of defects in ceramics, Am. Ceram. Soc. Bull. **97**, 16 (2018).

[26] F. Chen, Photonic guiding structures in lithium niobate crystals produced by energetic ion beams, J. Appl. Phys. **106**, 081101 (2009).

[27] S. Saremi, R. Xu, L. R. Dedon, J. A. Mundy, S.-L. Hsu, Z. Chen, A. R. Damodaran, S. P. Chapman, J. T. Evans, and L. W. Martin, Enhanced electrical resistivity and properties via ion bombardment of ferroelectric thin films, Adv. Mater. **28**, 10750 (2016).

[28] S. Saremi, R. Xu, L. R. Dedon, R. Gao, A. Ghosh, A. Dasgupta, and L. W. Martin, Electronic transport and ferroelectric switching in ion-bombarded, defect-engineered BiFeO$_3$ thin films, Adv. Mater. Interfaces **5**, 1700991 (2018).

[29] C. A. Volkert, and A. M. Minor, Focused ion beam microscopy and micromachining, MRS Bull. **32**, 389 (2007).

[30] L. J. McGilly, C. S. Sandu, L. Feigl, D. Damjanovic, and N. Setter, Nanoscale defect engineering and the resulting effects on domain wall dynamics in ferroelectric thin films, Adv. Funct. Mater. **27**, 1605196 (2017).

[31] J. Karthik, A. R. Damodaran, and L. W. Martin, Epitaxial ferroelectric heterostructures fabricated by selective area epitaxy of SrRuO$_3$ using an MgO mask, Adv. Mater. **24**, 1610 (2012).

[32] J. F. Ziegler, M.D. Ziegler, and J. P. Biersack, SRIM—The stopping and range of ions in matter, Nucl. Instr. Meth. Phys. Res. B **268**, 1818 (2010).

[33] See Supplemental Material at http://link.aps.org/supplemental/10.1103/PhysRevMaterials.2.084414 for full information about ferroelectric switching studies, first-order reversal curve analysis, band excitation piezoresponse force microscopy, structural and chemical analysis, SRIM simulations, and surface topography.

[34] A. Stancu, D. Ricinschi, L. Mitoseriu, P. Postolache, and M. Okuyama, First-order reversal curves diagrams for the characterization of ferroelectric switching, Appl. Phys. Lett. **83**, 3767 (2003).

[35] C. R. Pike, A. P. Roberts, and K. L. Verosub, Characterizing interactions in fine magnetic particle systems using first-order reversal curves, J. Appl. Phys. **85**, 6660 (1999).

[36] S. Jesse, and S. V. Kalinin, Band excitation in scanning probe microscopy: Sines of change, J. Phys. D. Appl. Phys. **44**, 464006 (2011).

[37] P. B. Johnson, D. J. Mazey, and J. H. Evans, Bubble structures in He$^+$ irradiated metals, Radiat. Eff. **78**, 147 (1983).

[38] M. Avrami, Kinetics of phase change. II Transformation-time relations for random distribution of nuclei, J. Chem. Phys. **8**, 212 (1940).

[39] Y. Ishibash, and Y. Takagi, Note on ferroelectric domain switching, J. Phys. Soc. Jpn. **31**, 506 (1971).

[40] J.Y. Jo, S. M. Yang, T. H. Kim, H. N. Lee, J.-G. Yoon, S. Park, Y. Jo, M. H. Jung, and T. W. Noh, Nonlinear Dynamics of Domain-Wall Propagation in Epitaxial Ferroelectric Thin Films, Phys. Rev. Lett. **102**, 045701 (2009).

[41] A. Chandrasekaran, D. Damjanovic, N. Setter, and N. Marzari, Defect ordering and defect-domain-wall interactions in PbTiO$_3$: A first-principles study, Phys. Rev. B **88**, 214116 (2013).

[42] U. Robels, and G. Arlt, Domain wall clamping in ferroelectrics by orientation of defects, J. Appl. Phys. **73**, 3454 (1993).

[43] W. L. Warren, G. E. Pike, K. Vanheusden, D. Dimos, B. A. Tuttle, and J. Robertson, Defect-dipole alignment and tetragonal strain in ferroelectrics, J. Appl. Phys. **79**, 9250 (1996).

[44] L. Zhang, E. Erdem, X. Ren, and R.-A. Eichel, Reorientation of (MnTi-VO$^{\bullet\bullet}$)$^\times$ defect dipoles in acceptor-modified BaTiO$_3$ single crystals: An electron paramagnetic resonance study, Appl. Phys. Lett. **93**, 202901 (2008).

[45] O. Boser, Statistical theory of hysteresis in ferroelectric materials, J. Appl. Phys. **62**, 1344 (1987).

[46] Y. Kadota, H. Hosaka, and T. Morita, Utilization of permittivity memory effect for position detection of shape memory piezoelectric actuator, Jpn. J. Appl. Phys. **47**, 217 (2008).